





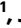






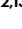



Electrochemiluminescent tactile visual synapse enabling in situ health monitoring

Received: 2 January 2024

Accepted: 1 January 2025

Published online: 24 February 2025

 Check for updates

Woojoong Kim ^{1,15}, Kyuho Lee ^{1,2,3,15}, Sanghyeon Choi ^{4,15}, Eunje Park ^{5,6}, Gwanho Kim ¹, Jebong Ha¹, Yeeun Kim¹, Jihye Jang¹, Ji Hye Oh¹, HoYeon Kim ¹, Wei Jiang ¹, Jioh Yoo ¹, Taebin Kim¹, Yeonji Kim ¹, Kwan-Nyeong Kim ⁵, Juntaek Hong⁷, Ali Javey ^{2,3}, Dong-wook Rha⁷, Tae-Woo Lee ^{5,6,8,9}, Keehoon Kang ^{5,6,10}, Gunuk Wang ^{11,12,13}  & Cheolmin Park ^{1,14} 

Tactile visual synapses combine the functionality of tactile artificial synapses with the ability to visualize their activity in real time and provide a direct and intuitive visualization of the activity, offering an efficient route for in situ health monitoring. Herein we present a tactile visual synapse that enables in situ monitoring of finger rehabilitation and electrocardiogram analysis. Repetitive finger flexion and various arrhythmias are monitored and visually guided using the developed tactile visual synapse combined with an electrical and optical output feedback algorithm. The tactile visual synapse has the structure of an electrochemical transistor comprising an elastomeric top gate as a tactile receptor and an electrochemiluminescent ion gel as a light-emitting layer stacked on a polymeric semiconductor layer, forming an electrical synaptic channel between source and drain electrodes. The low-power ($\sim 34 \mu\text{W}$) visualization of the tactile synaptic activity associated with the repetitive motions of fingers and heartbeats enables the development of a convenient and efficient personalized healthcare system.

The integration of displays into artificial synapses can create new types of neuromorphic device called visual synapses. They combine the functionality of artificial synapses with the ability to visualize their activity in real time^{1–3}. Visual synapses provide real-time and intuitive visualization of the activity of artificial synapses. This capability enables scholars to observe and analyse the behaviour of synapses as they process information, adapt and learn. Moreover, the development of motion-monitoring systems that enable direct communication

at human–device interfaces is enhanced by visual synapses^{4,5}. For instance, in a monitoring system that involves the motion of human bodies, the physical distance between an artificial synapse and an external communication device varies substantially from a few millimetres to centimetres, requiring lengthy electrical interconnects for long-distance communication^{6,7}. Visual synapses can mitigate these problems, making communication faster with low power consumption. Numerous examples of visual feedback are found in applications for

¹Department of Materials Science and Engineering, Yonsei University, Seoul, Republic of Korea. ²Electrical Engineering and Computer Sciences, University of California, Berkeley, CA, USA. ³Materials Sciences Division, Lawrence Berkeley National Laboratory, Berkeley, CA, USA. ⁴Department of Electrical and Computer Engineering, University of California, Santa Barbara, CA, USA. ⁵Department of Materials Science and Engineering, Seoul National University, Seoul, Republic of Korea. ⁶Research Institute of Advanced Materials, Seoul National University, Seoul, Republic of Korea. ⁷Department and Research Institute of Rehabilitation Medicine, Yonsei University College of Medicine, Seoul, Republic of Korea. ⁸Department of Chemical and Biological Engineering, Institute of Engineering Research, Interdisciplinary Program in Bioengineering, Soft Foundry, Seoul National University, Seoul, Republic of Korea. ⁹SN Display Co., Ltd., Seoul, Republic of Korea. ¹⁰Institute of Applied Physics, Seoul National University, Seoul, Republic of Korea. ¹¹KU-KIST Graduate School of Converging Science and Technology, Korea University, Seoul, Republic of Korea. ¹²Department of Integrative Energy Engineering, Korea University, Seoul, Republic of Korea. ¹³Center for Neuromorphic Engineering, Korea Institute of Science and Technology, Seoul, Republic of Korea. ¹⁴Post-Silicon Semiconductor Institute, Korea Institute of Science and Technology, Seoul, Republic of Korea. ¹⁵These authors contributed equally: Woojoong Kim, Kyuho Lee, Sanghyeon Choi. ✉e-mail: Gunukwang@korea.ac.kr; cmpark@yonsei.ac.kr

monitoring human protection and biomedical fields, such as assisting patients using visualized alarms to prevent acute arrhythmia^{8,9} and facilitating rehabilitation processes^{10,11}.

Sensory synapses capable of sensing and learning a wide range of stimuli, such as pressure^{12–16}, light^{17–21}, temperature^{22,23}, humidity^{24,25} and magnetic fields^{26,27}, have been demonstrated. These devices can be combined with various chromic and self-emitting materials that change their optical properties in response to electrical or chemical signals arising from artificial synapses. Visualization of an artificial synapse associated with various tactile stimuli, such as repetitive tapping and stretching, is of great importance for real-time motion tracking and revising^{12,16}. Various tactile visual synapses, comprising individual sensors, artificial synapses and light-emitting devices, have been reported. In some cases, they are physically interconnected with microprocessor units for facile signal conversion of those from the sensor and synapse into the display^{28–31}. However, these bulky tactile visual synapses are rarely suitable for real-time motion-monitoring and healthcare systems owing to their poor wearability on the body and high power consumption (Supplementary Table 1). Therefore, the development of a single-device tactile visual synapse is required, where tactile synaptic activity acquired by the device is directly visualized from the device. A single-device tactile visual synapse with full visible colour operation could further facilitate feedback-based diagnosis and rehabilitation with high accuracy.

We present a compact, low-power, full-colour, single-device electrochemiluminescent tactile visual synapse (ECL-TVS) inspired by a marine snail^{32,33}. The proposed ECL-TVS is based on a top-gate organic electrochemical transistor (OECT), comprising an elastomeric top gate as a tactile receptor, electrochemiluminescent ion gel as a light-emitting layer, and a polymeric semiconductor layer as a synaptic channel. While tactile motions imposed on the top gate are represented by the synaptic current of the semiconducting channel as a function of the degree and frequency of the tactile motions, the synaptic activity is visualized in the electrochemiluminescent ion gel. An energy-efficient (~ 3 V, ~ 34 μ W) wearable ECL-TVS panel capable of monitoring subtle distal motions of fingers, in which the repetitive finger flexion (and extension) motions are monitored and visually guided using our thin wearable ECL-TVS in combination with the electrical and optical output feedback algorithm, is demonstrated. Furthermore, various types of arrhythmia, which are unwanted irregular heartbeats, are visually monitored and interpreted in real time using a spiking neural network (SNN). The ECL-TVS serves as a convenient and effective platform for personalized healthcare by enabling the monitoring of repetitive finger movements and heartbeats. We validate its utility as a tool for in situ monitoring by observing functional enhancements in users' finger movements and the high accuracy of electrocardiogram (ECG) data analysis facilitated by the ECL-TVS.

Results

Electrochemiluminescent tactile visual synapse (ECL-TVS)

Hinea brasiliana, a glowing sea snail, processes a tactile sensory synaptic display (chemiluminescence) that protects it from predators, as schematically shown in Fig. 1a. The tactile sensory synaptic display of a sea snail involves the tactile receptor (Fig. 1a(i)), neurotransmission at the synapse (Fig. 1a(ii)) and the light-emitting cell (Fig. 1a(iii)) (Supplementary Note 1). Inspired by the touch-responsive synaptic chemiluminescence of the sea snail, we developed a full-colour single-device ECL-TVS based on a top-gated bottom-contact OECT with a mechanically deformable elastomeric top gate, as schematically shown in Fig. 1b. The ECL-TVS is composed of interdigitated indium tin oxide (ITO) source/drain electrodes, and a thin poly(3-hexylthiophene-2,5-diyl) (P3HT) film approximately 50 nm in thickness. On top of the P3HT layer, an approximately 750- μ m-thick ion gel, which is composed of a poly(vinylidene fluoride-co-hexafluoropropylene) (P(VDF-HFP)) matrix and an ionic liquid—1-butyl-1-methylpyrrolidinium bis(trifluoromethylsulfonyl)

imide ([PYR₁₄][TFSI])—containing co-reactant tripropylamine (TPRA) and luminophores, is placed using the 'cut-and-stick' method³⁴. The device utilizes three representative luminophores: Ru(bpy)₃Cl₂, Ir(dFppy)₂(bpy)PF₆ and Ir(dFppy)₂(pic) (Firpic) for red, green and blue ECL, respectively. The top layer contains a mechanically deformable, hemisphere-shaped elastomeric polydimethylsiloxane (PDMS) gate, coated with a thin Cr/Au film. The detailed fabrication process is shown in Supplementary Fig. 1.

An ECL-TVS emulates the tactile visual synapse of a sea snail in a single-device platform. As depicted in Fig. 1c(i), a deformable hemisphere top gate serves as a mechanoreceptor. The P3HT channel current corresponds to synaptic properties, as schematically shown in Fig. 1c(ii). Electrochemiluminescence (ECL) in the ion gel replicates light emission observed in sea snails, as depicted in Fig. 1c(iii). Direct full-colour ECL visualization of the synaptic activity was achieved by the proper formulation of the ionic liquid ([PYR₁₄][TFSI]), co-reactant (TPRA) and luminophores (R, G and B) in the electrically robust dielectric polymer, P(VDF-HFP). The homogeneous mixing of reactant and luminophores in an ion gel was confirmed using X-ray photoelectron spectroscopy as well as two-dimensional grazing-incidence wide-angle X-ray scattering (Supplementary Figs. 2 and 3). The contact area of the hemisphere top gate on the ion gel was controlled by applying pressure (~ 12.51 kPa), resulting in a contact diameter of ~ 2 mm (Fig. 1d). The left inset in Fig. 1d is a photo of a circular-shaped ion gel layer containing three pieces of ion gels with red, green and blue luminophores. The right inset in Fig. 1d shows an interdigitated source/drain electrode pattern. The cross-section of an ECL-TVS was examined using a scanning electron microscope combined with energy-dispersive X-ray spectroscopy (EDX), and the results show that all the constituent layers are uniformly laminated (Supplementary Fig. 4).

In the proposed ECL-TVS, the electrical synaptic activity is represented by the lateral P3HT channel current, while the visualization of the synaptic activity results from the electrochemical reaction in the ion gel sandwiched between the top gate and P3HT channel (see Supplementary Figs. 5 and 6 for photographs of full-colour ECL and its mechanism). The ECL spectra illustrated in Fig. 1e confirm the full-colour emission from the ECL-TVSs with the wavelengths at the maximum intensities of approximately 620 nm, 543 nm and 474, 493 nm for R, G and B luminophores, respectively. We examined the electrical transfer and luminance characteristics of the ECL-TVSs as a function of the gate voltage, and the results are presented in Fig. 1f. The three types of ECL-TVS demonstrate similar transfer curves, with an ON/OFF current ratio of approximately 1.13×10^4 . Moreover, they show electrical hysteresis owing to the presence of the ionic liquids [PYR₁₄][TFSI] in the ion gels^{35,36}. A maximum brightness of approximately 37.82 cd m⁻² was achieved in an ECL-TVS (Fig. 1f) (Supplementary Fig. 7).

As shown in Fig. 1g, the electrical threshold voltages for the R, G and B ECL-TVS devices are approximately -0.46 V, -0.53 V and -0.37 V, respectively. The corresponding threshold voltages for light emission are approximately -2.47 V, -3.43 V and -2.81 V. The results confirm that the threshold voltages for R, G and B emissions depend on the oxidation potentials of the co-reactant and luminophores^{37,38}. Notably, the ionic liquid [PYR₁₄][TFSI] employed in the ECL-TVS devices exhibits a wider chemical stability window than do other ionic-liquid-based ion gels. We conducted a comparative analysis with 11 additional ionic liquids commonly used for ionic device applications (Supplementary refs. 16–32, Supplementary Fig. 9 and Supplementary Table 2). Among the tested ionic liquids, [PYR₁₄][TFSI] exhibited the largest electrochemical window of approximately 5 V, enabling the stable operation of R, G and B ECL, as explicitly described later.

Analysis of the operational mechanism in an ECL-TVS

The synaptic current from the P3HT channel and ECL in the ionic gel associated with the mechanical touch events occurred as follows: (1) electric double layer formation and anion doping into the P3HT

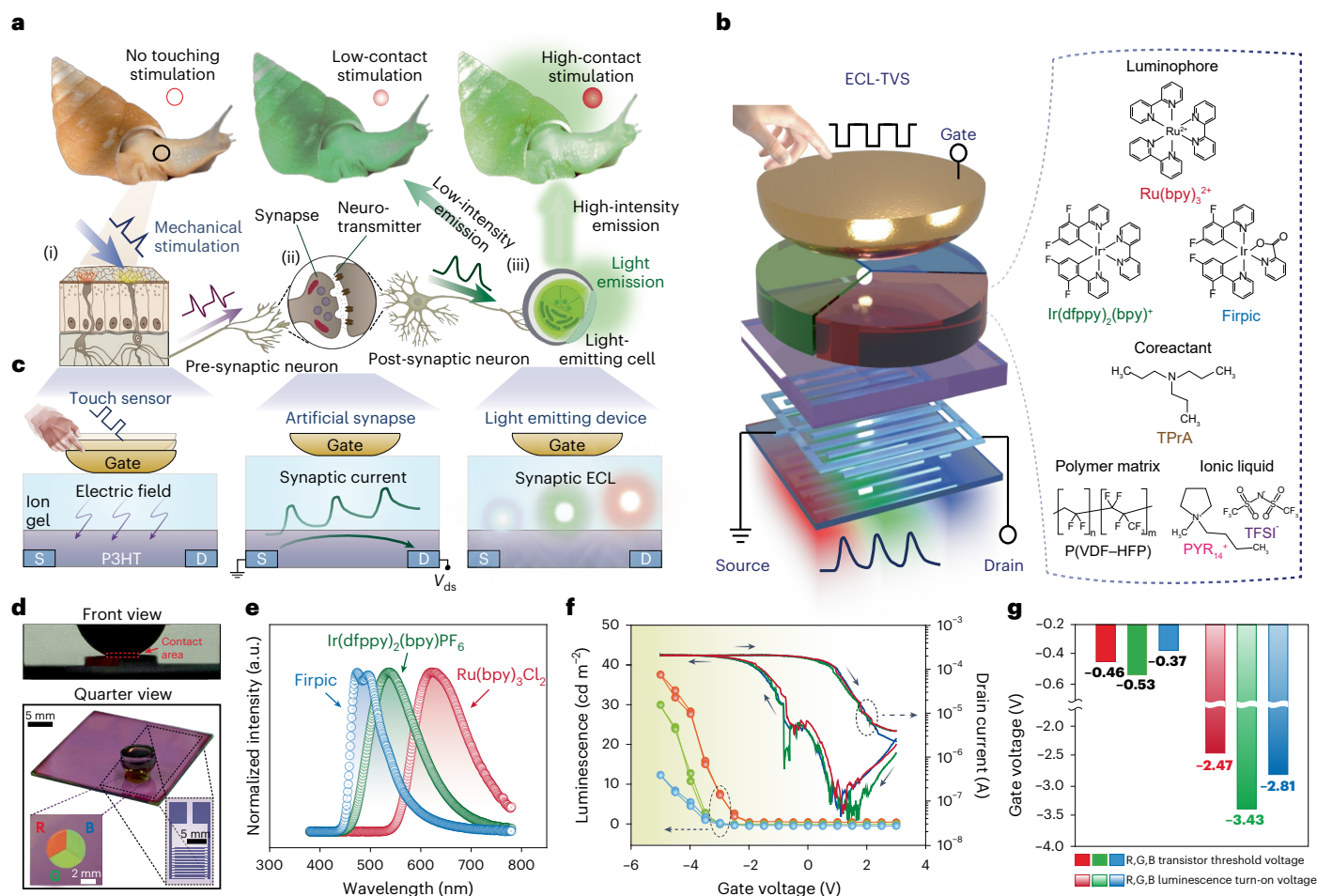


Fig. 1 | Electrochemiluminescent tactile visual synapse (ECL-TVS). **a, c**, Schematic of the sea snail's biological tactile perception and bioluminescent system: (i) the tactile sensory receptors, (ii) synapse and (iii) light-emitting cell (photocyte) in the epithelial tissue of the glowing sea snail (a) and the corresponding ECL-TVS based on an ion-gel-gated device (c). **b**, Device structure of ECL-TVS and the components that make up the electrochemiluminescent ion gel. **c** (i), Artificial tactile sensors with dome-shaped elastomeric gate electrode and ion gel dielectric layer below it; (ii) artificial synapse showing synaptic currents between source (S) and drain (D) electrodes; (iii) artificial light-emitting

cell with ion gel containing luminophore and co-reactant, which generate light through electrochemiluminescence. **d**, Photograph of the ECL-TVS device from the front view and quarter view. Front view: gate electrode pressing the ion gel. Quarter view: ECL-TVS device and the pressure-sensitive gate electrode. Insets: photograph of full-colour light-emitting ion gel and schematic of the ITO source/drain electrode. **e**, Normalized R, G and B ECL-TVS emission spectra. a.u., arbitrary units. **f, g**, Electrical transfer and luminance characteristics of the ECL-TVSs as a function of gate voltage (f) and the threshold voltages for electrical transistor and emission of the three ECL-TVSs with R, G and B luminophores (g).

channel, (2) polaron generation, (3) enhanced conductance of the P3HT channel and (4) ECL emission in the ion gel correlated with the enhanced P3HT channel conductance, as schematically illustrated in Fig. 2a. When a negative pulse was imposed on an ECL-TVS, the electric double layer was instantly developed at the ionic gel, including [PYR₁₄][TFSI] with a P3HT channel, followed by the doping of TFSI anions into the P3HT channel. Simultaneously, holes injected from an ITO drain electrode produced polaron pairs of holes, enhancing the channel conductance. The increased conductance boosted the drain–source current (I_{ds}) at a drain–source voltage (V_{ds}) of -0.1 V. Consecutive gate pulses further increased the channel current due to cumulative polaron accumulation, resulting in the characteristic synaptic long-term potentiation behaviour (Supplementary Figs. 10–13). ECL originates from a redox reaction of luminophores in the ion gel, initiated by a capacitive voltage greater than the threshold redox voltage of the luminophores. In addition, since the redox reaction occurs at the interface between the ion gel and the P3HT channel, the P3HT channel should supply a sufficient number of hole carriers to facilitate the interface redox reaction, which should correlate with the electrical conductance of the ion-gel-gated P3HT channel. The close link between the synaptic behaviour (that is the electrical device characteristics) and the gate-pulse-dependent

ECL behaviour enables direct visualization of the electrical synaptic properties.

To quantitatively assess the mechanistic details of the ECL synaptic behaviours, we first performed an in situ spectroelectrochemical experiment to support our speculation of the ECL being dependent upon the synaptic P3HT channel current. The spectral signatures of polaronic states in the P3HT channel were monitored in real time for gate bias ranging from -0.2 to -1.2 V versus Ag/Ag^+ , as schematically shown in Fig. 2b (Supplementary Fig. 14). As shown in Fig. 2d, a broad absorption peak from 750 nm to 1,100 nm increased with gate voltage, corresponding to the increase in the polaronic absorption, while neutral P3HT absorption (~ 500 nm) decreased.

Furthermore, we measured the gate current to quantitatively calculate the hole concentration (number of holes injected per unit volume) in response to gate potentials ranging from -0.2 to -1.2 V (Fig. 2e). The hole concentration was calculated by integrating the gate current over time using the relation hole concentration = $\frac{1}{eWLd} \int_{t_1}^{t_2} I(t)_{\text{gate}} dt$, where e denotes the elementary charge and W , L and d denote the channel width, length and thickness, respectively. As shown in Fig. 2f, similar to the results from the

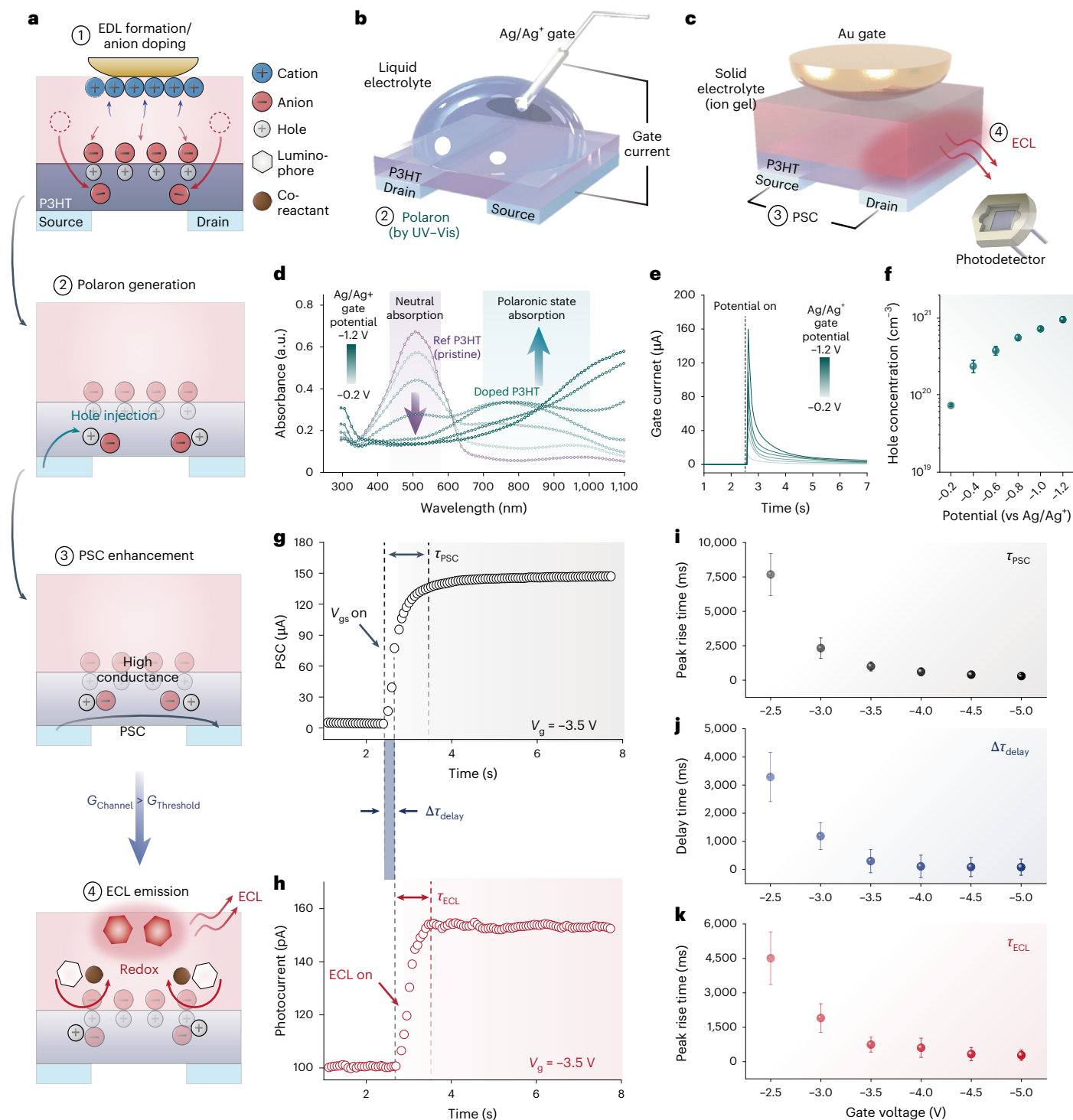


Fig. 2 | Analysis of the operational mechanism in an ECL-TVS. **a**, Schematic illustration of the operational mechanism in an ECL-TVS. EDL, electric double layer. **b, c**, Schematic illustrations of liquid-electrolyte- (**b**) and solid-electrolyte-based (**c**) in situ measurement systems, with corresponding results shown in **d–f** and **g–k**, respectively. **d**, Absorbance plots of the P3HT layer as a function of doping potential. **e**, Plots of transient gate current of the P3HT film with different applied doping potentials. **f**, Calculated hole concentration from **e**. **g, h**, Real-time

plots of PSC (**g**) and ECL photocurrent (**h**) under the gate bias of -3.5 V in solid-electrolyte-based ECL-TVS. The rise times of PSC (τ_{PSC}) and ECL (τ_{ECL}) represent the timespans between 10% and 90% of the maximum values, while the ECL delay time ($\Delta\tau_{\text{delay}}$) is the delay from V_{gs} (gate–source voltage) application to ECL emission. **i–k**, Plots of rise time of PSC (**i**), delay time (**j**) and rise time of ECL (**k**) as functions of applied gate voltage. Error bars in (**f, i–k**) represent mean \pm s.e.m., calculated from technical replicates ($n = 6$).

spectroelectrochemical measurements (Fig. 2d), the number of generated hole polarons increased with the gate potential. The hole carrier concentration reached approximately 10^{21} cm^{-3} at a gate bias of -1.2 V, comparable to the hole concentration typically observed in bulk-doped channels of OECTs^{39,40}. Therefore, we can suspect that a high degree of

doping of the P3HT channel is a necessary condition for the observed ECL emission to occur in our devices (Supplementary Figs. 15 and 16).

In situ monitoring of the source–drain current and ECL intensity with time was performed as a function of gate bias from -2.5 to -5 V in an ECL-TVS (ion gel based), as schematically shown in Fig. 2c. Both

source–drain current and ECL were increased with time at a given gate voltage of -3.5 V, as shown in Fig. 2g,h, respectively. The rate at which the postsynaptic current (PSC) saturated increased with the gate bias, as shown in Fig. 2i, which is qualitatively consistent with the in situ spectroelectrochemistry results that directly indicate the degree of polaron formation by TFSI⁻ doping (Supplementary Figs. 17 and 18). The rate at which ECL emission intensity saturated also increased with the gate bias, as shown in Fig. 2k. Overall, the results from the spectroelectrochemistry, PSC and ECL all indicate that ECL is closely related to the P3HT channel conductance governed by the polaron density generated from TFSI⁻ ion doping and the level of hole injection from the drain electrode. (See Supplementary Note 2 for the Butler–Volmer equation in ECL-TVS.)

Interestingly, we observed that there was a delay in the onset of ECL emission (Fig. 2h), $\Delta\tau_{\text{delay}}$, from the onset of the PSC channel at a given gate bias (Fig. 2g). More specifically, ECL occurred approximately 300.4 ms after the channel current onset at the gate bias of -3.5 V. This reflects the extra time required to reach a certain channel conductance (and therefore polaron density in the channel) before initiating ECL emission. $\Delta\tau_{\text{delay}}$ decreased with increasing gate bias (Fig. 2j), until ECL emission was simultaneously activated from the gate bias of -4 V (Supplementary Fig. 19). Additionally, the origin of the current between the top gate and the bottom source/drain electrode (J_{gs}) of an ECL-TVS, which is responsible for ECL, was further analysed with a set of OECTs with different components (Supplementary Fig. 20).

Visualization of the tactile synaptic activity in an ECL-TVS

The tactile synaptic activity was visualized in an R-ECL-TVS, as shown in Fig. 3a,b. Specifically, a constant negative gate voltage of -3.5 V was applied to the ECL-TVS, sufficiently large for the oxidation of the Ru(bpy)₃²⁺ and TPRA, which in turn triggered the ECL reaction. The level of PSC and ECL increased with the number of applied gate tactile pulses, as shown in Fig. 3a. The redox current data of our ECL-TVS were obtained by subtracting the ionic doping current associated with the P3HT channel current from the total gate current (Supplementary Fig. 21). The redox current qualitatively correlates with the transient ECL brightness, supporting the ECL-TVS mechanism (Fig. 3a,c and Supplementary Fig. 22).

The synaptic plasticity of the device at different tactile pulse frequencies was examined, and the results are shown in Fig. 3c. The PSC level increased in dependence on the gate tactile frequency in the order of 0.2 Hz, 0.5 Hz and 2.0 Hz, which is consistent with the results for synaptic plasticity at different electrical pulse frequencies (Supplementary Fig. 11c). The light intensity paired-pulse facilitation (I-PPF) and emitting area paired-pulse facilitation (A-PPF) are plotted as a function of the tactile pulse frequency, as shown in Fig. 3d,e, respectively. The ECL-TVS of this study exhibits an increase in the light-emitting area with the number and frequency of tactile pulses (Fig. 3b,e). These unique results in the light-emitting area arose from the gate-electric-field-dependent ECL reaction in a thick volumetric ion gel with a thickness of approximately 750 μm , as schematically illustrated in Fig. 3f. Following consecutive gate pulses, the area of ECL was controlled by the asymmetric electric field between the top gate and bottom drain electrode developed by the geometric design of both electrodes and the ion gel. Numerical simulations of the electric field distribution in our ECL-TVS were conducted using finite-element analysis, as depicted in Fig. 3g (see Supplementary Fig. 23 for the symmetric (flat-contact) case). In particular, in the ECL-TVS developed in this study, the area between the P3HT and ion gel is larger (5 mm) than that of the gate electrode (2 mm), and the capacitance of the device was notably increased with ion gel thickness (Fig. 3h). In this ‘asymmetric-geometry capacitor’ situation, the light emission area was readily controlled by varying the relative dimensions of the two electrodes and the thickness of the ion gel, as shown in Fig. 3f,g (Supplementary Note 3 and Supplementary Figs. 24–26). The full-colour

ECL-TVS operation, which will later be utilized in the application, is described in Extended Data Fig. 1, Supplementary Note 4 and Supplementary Video 1.

Finger rehabilitation monitoring with a wearable ECL-TVS

We developed a personalized wearable device to help with the rehabilitation of various finger motions (Supplementary Fig. 28) facilitated with an ECL-TVS (Supplementary Note 5). We emphasized the functional rehabilitation of finger bending, a crucial function in daily life for actions such as writing, typing and grasping. As shown in Fig. 4a, ECL-TVSs were fabricated with red, green and blue ECL chromophores on a glass substrate, followed by being vertically fixated on a palm (see Methods for detailed fabrication of the wearable ECL-TVS). The positions of three ECL-TVSs on the rehabilitation panel were optimized for finger contact. They were determined on the basis of a personalized hand recognition algorithm combined with image analysis, and the results are shown in Fig. 4b (Supplementary Fig. 29). After coordination was completed, red, green and blue ion gels were carefully placed on the obtained coordinates, as shown in Fig. 4b. Personalized finger position recognition coding was also performed, allowing reliable ECL emission upon finger contact events (Supplementary Figs. 30 and 31).

We examined the bending of the index, middle and ring fingers. The electrical threshold of 0.13 mA was consistent across all fingers, with ECL thresholds set at 1.45×10^6 Σ brightness for the index finger, 1.3×10^6 Σ brightness for the middle finger and 9×10^5 Σ brightness for the ring finger, achievable with ten moderate taps (12.51 kPa) (see Supplementary Fig. 32 for rehabilitation monitoring, and Supplementary Fig. 33 for the exercise programme). As shown in Fig. 4c,d, the electrical and ECL output data were collected when the index, middle and ring fingers were successfully tapped on the wearable panel 12, 8 and 4 times, respectively. Both electrical and ECL output (see Supplementary Fig. 34 for brightness extraction algorithm) were intensified with the taps, as shown in Fig. 4c,d, respectively (Supplementary Video 2). As expected, only the index finger, with its 12 successful taps via proximal interphalangeal joint motions, exceeded both the electrical and ECL thresholds. Eight and four taps of the middle and ring finger bending motions on the panel were not sufficiently large to reach the threshold values. When the exercise was performed adequately with all three fingers, both electrical and ECL results successfully exceeded the threshold values (Supplementary Fig. 35). Furthermore, this method successfully tracked the rehabilitation progress and provided visualized feedback to users immediately (Supplementary Note 6 and Supplementary Figs. 36 and 37).

Notably, the developed wearable rehabilitation device consumes power only when a finger exercise is performed with 12 discrete events (for example, finger bending motions). On the basis of the 12 consecutive cycles shown in Fig. 4c, the total energy consumption of one person for a five-week rehabilitation period is 84 mJ (Supplementary Fig. 38). An experiment was conducted to assess the feasibility of utilizing the ECL-TVS as a wearable device capable of operating with four standard portable batteries. (Supplementary Fig. 39 and Supplementary Video 3). Long-term performance of the ECL-TVS connected with a soft actuator was examined (Supplementary Figs. 40–42).

Arrhythmia monitoring with ECL-TVS

We also demonstrate that our full-colour ECL-TVS is suitable for monitoring and directly visualizing various types of arrhythmia with different ECL colours, combined with an SNN, and the results are shown in Fig. 5. The MIT-BIH arrhythmia dataset was employed (Fig. 5a) to perform the prompt visualization of arrhythmia status⁴¹. The dataset contains ECG signals corresponding to either normal or abnormal heartbeats. As shown in Fig. 5a, the ECG signals exhibit unique shapes and features of heartbeats over time, which can be labelled into five representative classes: ‘N’, ‘S’, ‘V’, ‘F’ and ‘Q’. The N class indicates a healthy state, whereas the remaining classes represent types of arrhythmia.

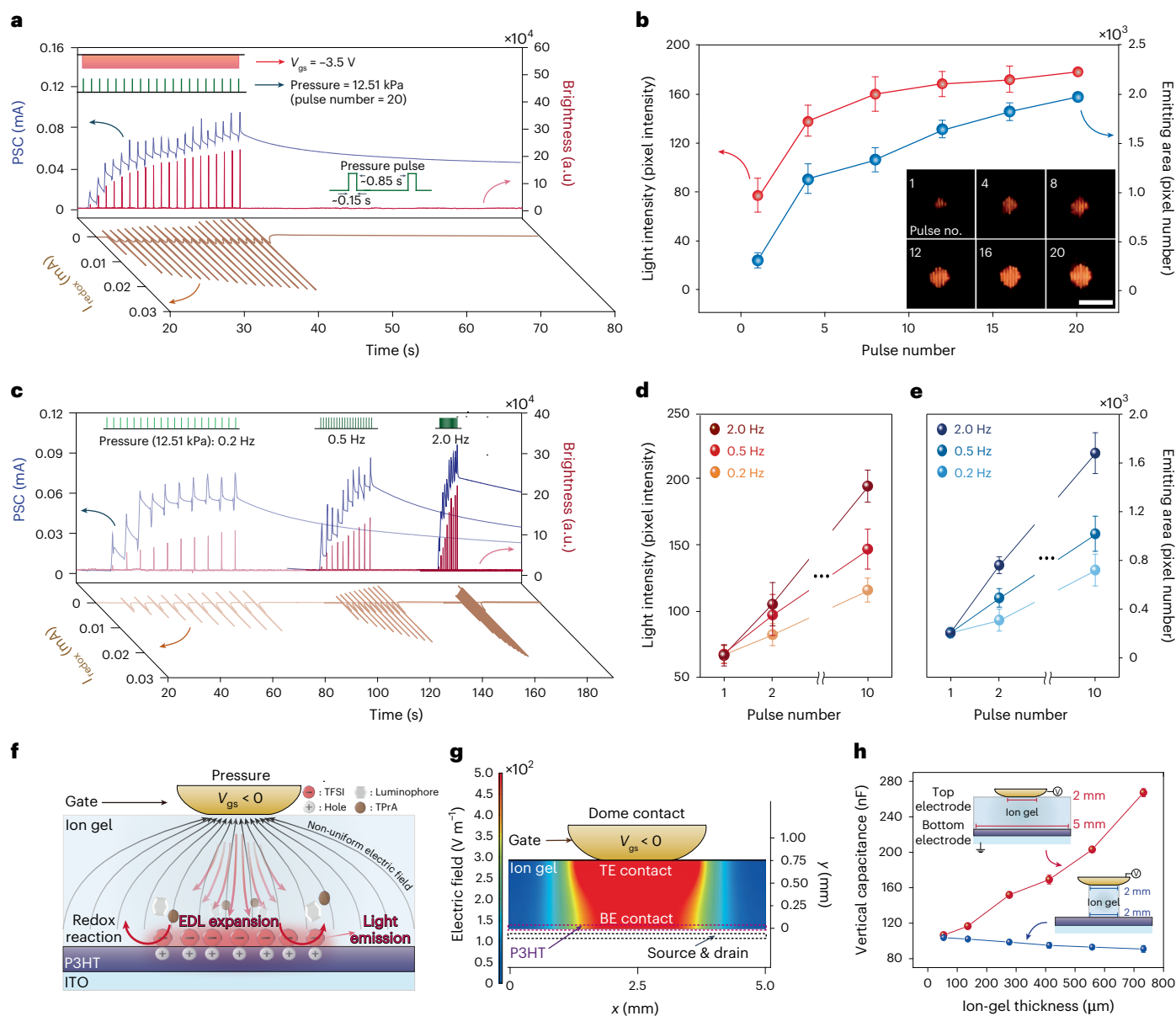


Fig. 3 | Visualization of the tactile synaptic activity in an ECL-TVS. a, Plots of the PSC response, the brightness and the redox current of an R-ECL-TVS with 20 tactile pulses under a continuously applied negative gate voltage ($V_{gs} = -3.5$ V, $V_{ds} = -0.1$ V, pressure pulse duration = 0.15 s and pressure pulse interval = 1 s). **b**, Plots of the light intensity and light-emitting area of the R-ECL-TVS from a with inset photographs displaying the ECL at the 1st, 4th, 8th, 12th, 16th and 20th tactile pulses. Scale bar: 5 mm. **c**, Plots of the PSC response, the brightness and the redox current of an R-ECL-TVS at different frequencies of pressure pulses.

d, e, Light intensity (**d**) and emitting area (**e**) at first, second and tenth pulses at pressure frequencies of 0.2 Hz, 0.5 Hz and 2 Hz. **f**, Schematic illustration of the electric field for a dome-shaped gate electrode and light emission of the ECL-TVS. **g**, Finite-element analysis simulation of the electric field distribution in the ECL-TVS with a dome-shaped electrode contact. TE, top electrode; BE, bottom electrode. **h**, Plots of capacitance as a function of ion gel thickness when the lateral dimension of the ion gel was 2 mm and 5 mm, respectively.

Additional dataset information is given in Supplementary Table 3 and Methods. Figure 5b shows a diagnostic flow example of an SNN based on an ECL-TVS with respect to V . The SNN, which closely emulates the operating principle of the human brain, operates on the basis of the sequence and timing of spikes, thereby facilitating time-series information processing, such as an ECG signal, with high energy efficiency when compared with artificial neural networks⁴².

As shown in Fig. 5b, the SNN contains synapses fully connected between pre- and post-neurons (Supplementary Figs. 43 and 44 and Methods). Here, we applied the ECL-TVS as both synapses and post-neurons on the basis of its synaptic, tactile and ECL functionalities (Supplementary Fig. 45). When an ECG signal enters the network, pre-neurons transform their temporal inputs into sparse

electrical spike trains (V_{pre}). The post-neurons collect and integrate the incoming spikes from pre-neurons, which are scaled by the strength of the synaptic connection (that is, synaptic weight, w). If the sum of the weighted spikes (wV_{pre}) over time at a certain post-neuron ($V(t)$) exceeds a threshold, the post-neuron fires an output spike (V_{post}) and then visualizes the diagnostic results with ECL (Supplementary Fig. 45). Figure 5c shows experimental demonstrations of spike-timing-dependent plasticity (STDP) obtained from an ECL-TVS as a function of pressure. STDP, which is a fundamental learning rule of the brain, can determine the change in the synaptic weight (Δw) on the basis of the relative spike timing of the pre- (t_{pre}) and post-neuron (t_{post}) ($\Delta t = t_{post} - t_{pre}$; ref. 42). Despite the application of the same input voltage scheme (left inset of Fig. 5c), the STDP can be further

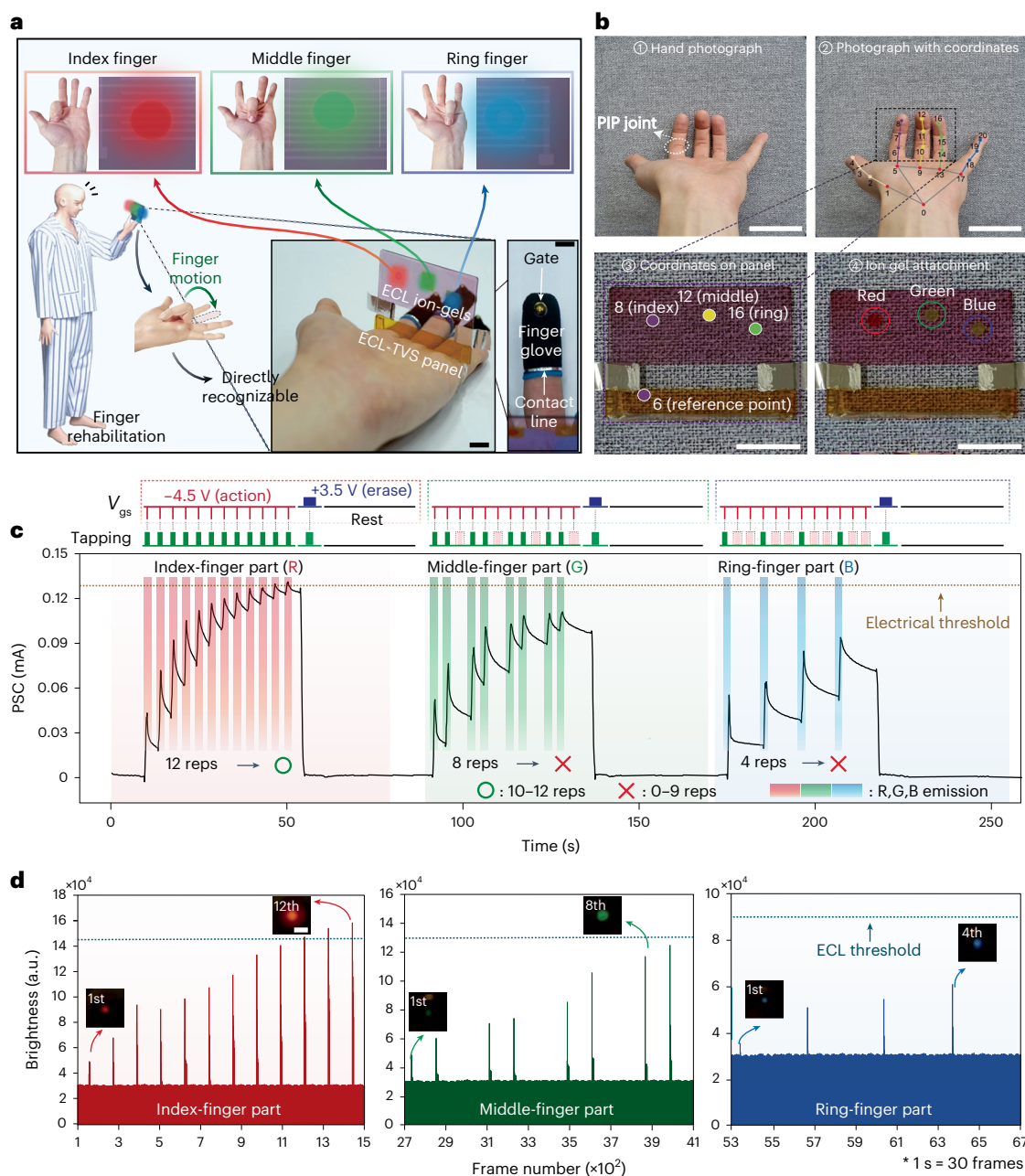


Fig. 4 | Finger rehabilitation monitoring with a wearable ECL-TVS. a, Schematic illustration of finger rehabilitation exercise for index, middle and ring fingers. Left inset: photograph of a personalized wearable finger rehabilitation ECL-TVS panel. Right inset: photograph of a finger cap made of a lightweight rubber film with an elastomeric hemispherical top gate. Scale bar: 5 mm. **b**, Personalized rehabilitation equipment and hand recognition algorithm process through image analysis. Scale bars: 5 cm (upper panels), 2.5 cm (lower panels). PIP, proximal interphalangeal joint. **c**, Plots of electrical output of the ECL-TVS

during the exercise for the index finger, middle finger and ring finger. Duration of tapping = 1.5 s, interval of tapping = 4 s and gate voltage at each tapping action = -4.5 V were used during cycles of tapping action. In contrast, erasing gate voltage = +3.5 V was used to return the device to the initial state. **d**, Plots of the ECL output during exercises corresponding to **c**. Insets: photographs of emissions of the initial and final states of the index finger, middle finger and ring finger. Scale bar: 2 mm.

modulated on the basis of the applied pressure. This result indicates that the external pressure inputs enable the in situ alternation of STDP behaviour, which can be utilized as a tunable learning parameter (Supplementary Table 4).

Figure 5d,e shows firing frequencies of different post-neurons before and after STDP learning over timesteps at 12.51 kPa. Note that N, S, V, F and Q are sequentially entered into the network every 100 timesteps (top of Fig. 5d,e). Before learning (Fig. 5d), the post-neurons are observed to fire irregularly regardless of the incoming ECG classes, indicating complete failure of diagnosis (accuracy ~12%). However,

after the learning (Fig. 5e), each post-neuron fires only when the corresponding ECG class enters the network, exhibiting a considerable improvement in diagnostic accuracy (~84%). The output spikes are then utilized to implement ECL, allowing the diagnostic results to be readily visualized and confirmed (Fig. 5b and Supplementary Fig. 45). Figure 5f shows a change in the diagnostic accuracy with respect to different pressures. Considering that the normal resting blood pressure of an adult ranges from 11 kPa to 16 kPa, the suggested SNN could potentially be extended to on-skin wearable healthcare devices (Supplementary Note 7).

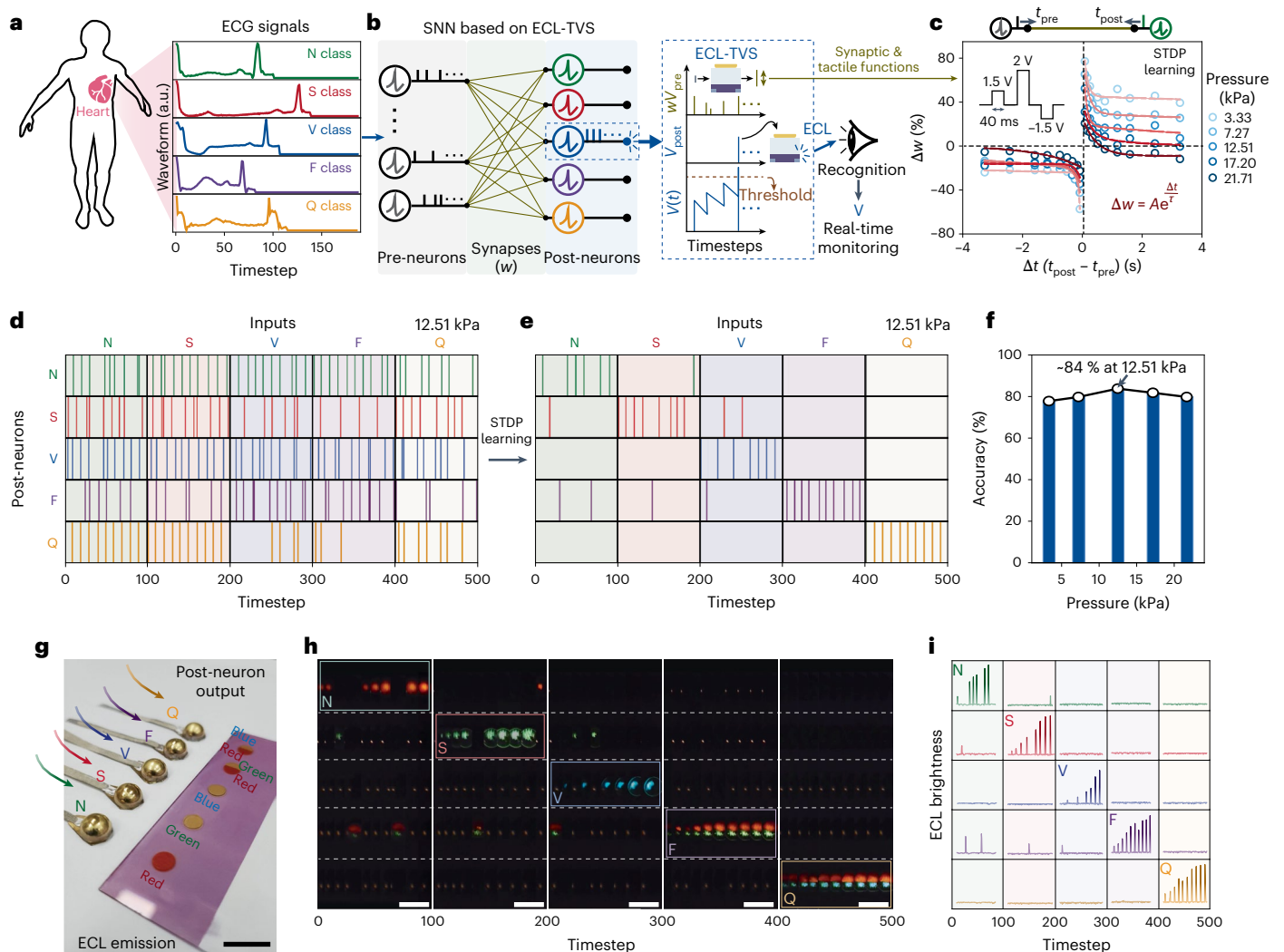


Fig. 5 | Arrhythmia monitoring system with ECL-TVS. **a**, A schematic illustration of the five representative classes of ECG signals from the heart: N, S, V, F and Q. **b**, A diagnostic flow and its visualization process based on an SNN comprising pre- and post-neurons connected by synapses, when receiving V-class signal. Inset (blue dotted lines): the operation schemes that show the utilization of ECL-TVS within the SNN. The ECL-TVS can scale V_{pre} from various pre-neurons with the synaptic and tactile functions (wV_{pre}), accumulating over time as $V(t)$ in the corresponding post-neuron. Once $V(t)$ reaches a threshold, V_{post} is fired and transmitted as input for ECL visualization of the diagnostic result, enabling real-time ECG monitoring. **c**, Plots of STDP learning behaviours of the ECL-TVS as a function of external pressure inputs. Δw increases when the designed voltage pulse scheme consisting of 1.5 V, 2 V and -1.5 V with a width of 40 ms is applied to

both the pre- and post-neuron with a smaller Δt and a stronger pressure. All the plots follow exponential STDP curves (red dashed lines). **d, e**, Plots of V_{post} over timesteps of the SNN based on the ECL-TVS before (**d**) and after STDP learning (**e**) in response to different ECG classes at 12.51 kPa. The sequence of applied input classes is shown at the top. **f**, Diagnostic accuracies of the ECG signals after the STDP learning as a function of the applied pressure. For 12.51 kPa, the estimated diagnostic accuracy is observed to achieve its optimal value (~84%). **g**, A photograph of the experimental set-up for the direct visualization process of diagnostic results. Scale bar: 1 cm. **h**, Photographs of ECL emission over timesteps at each post-neuron after STDP learning. This diagnostic result corresponds to **e**. Scale bar: 1 cm. **i**, Plots of the ECL output over timesteps at each post-neuron, which reflects and quantifies the ECL emission in **h**.

The direct visualization of the trained post-neuron output spikes of N, S, V, F and Q (Fig. 5e) was achieved using five ECL-TVSs with ECL luminophores of red, green, blue, red/green and red/blue, as shown in the photograph in Fig. 5g. For the visualization of post-neurons for F and Q inputs, we employed an ECL layer containing hemicircles of red/green and red/blue, respectively. The post-neurons mostly corresponding to N inputs during the time step from 0 to 100 were visualized in an ECL-TVS with red luminophores responsible for N inputs, as shown in Fig. 5h. Similarly, the post-neurons for S, V, F and Q inputs were successfully visualized in ECL-TVSs with green, blue, red/green and red/blue ECL, as shown in Fig. 5h. The intensified ECL with the time-sequential post-neurons of N, S, V, F and Q is quantified in Fig. 5i. This demonstration suggests a framework for real-time arrhythmia detection and visualization application with

a full-colour ECL-TVS, promising an intelligent healthcare display at the edge.

Discussion

We have demonstrated that a tactile visual synaptic device is potentially suitable for electrically and optically monitoring movements of body parts, offering a broad range of healthcare applications, including personalized therapy, intelligent healthcare and physiological monitoring. An ECL-TVS was developed based on a top-gated OECT, and its emission was conveniently modulated in the full visible range with the gate voltage of the device. The study revealed that the synaptic current from the semiconducting channel was correlated with luminescence from the ionic gel upon a pulsed gate field associated with the mechanical touch events. Sensing, learning and visualization of

various tactile events were power-efficiently (~34 μW) accomplished in the tactile visual synapse. Remarkably, the wearable tactile visual synapse suited to a palm and a finger promotes the rehabilitation of the finger, enabling efficient tracking of the progress in both electrical and optical modes. Furthermore, advanced physiological monitoring with SNN learning of ECG data was demonstrated. The integration of embedded electronics with advanced machine learning algorithms could enable more predictive analytics, offering pre-emptive adjustments to therapy protocols based on patient-specific data trends. This motion-monitoring device with visual feedback based on an artificial visual synapse sets a promising foundation for future research and development in various biomedical applications while exploring new light-emitting materials and device configurations.

Online content

Any methods, additional references, Nature Portfolio reporting summaries, source data, extended data, supplementary information, acknowledgements, peer review information; details of author contributions and competing interests; and statements of data and code availability are available at <https://doi.org/10.1038/s41563-025-02124-x>.

References

- Chen, Y. et al. Synaptic plasticity powering long-afterglow organic light-emitting transistors. *Adv. Mater.* **33**, 210369 (2021).
- Zhu, Y. et al. Intelligent, biomimetic, colour-tunable, light-emitting artificial skin with memory function. *Nano Energy* **90**, 106569 (2021).
- Zhao, S. et al. Electroluminescent synaptic devices with logic functions. *Nano Energy* **54**, 383–389 (2018).
- Seung, H. et al. Integration of synaptic phototransistors and quantum dot light-emitting diodes for visualization and recognition of UV patterns. *Sci. Adv.* **8**, eabq3101 (2022).
- Zhu, Y. et al. Light-emitting memristors for optoelectronic artificial efferent nerve. *Nano Lett.* **21**, 6087–6094 (2021).
- Cai, M. et al. A multifunctional electronic skin based on patterned metal films for tactile sensing with a broad linear response range. *Sci. Adv.* **7**, eabl8313 (2021).
- Zhang, L. et al. Wearable circuits sintered at room temperature directly on the skin surface for health monitoring. *ACS Appl. Mater. Interfaces* **12**, 45504–45515 (2020).
- Luigi, D. et al. Visual, tactile, and contact force feedback: which one is more important for catheter ablation? Results from an in vitro experimental study. *Heart Rhythm* **11**, 506–513 (2014).
- Dobiasch, M., Krenn, B., Lamberts, R. P. & Baca, A. The effects of visual feedback on performance in heart rate- and power-based-tasks during a constant load cycling test. *J. Sports Sci. Med.* **21**, 49–57 (2022).
- Elor, A. & Kurniawan, S. The ultimate display for physical rehabilitation: a bridging review on immersive virtual reality. *Front. Virtual Real.* **1**, 585993 (2020).
- Viirre, E. & Sitarz, R. Vestibular rehabilitation using visual displays: preliminary study. *Laryngoscope* **112**, 500–503 (2002).
- Lee, K. et al. Artificially intelligent tactile ferroelectric skin. *Adv. Sci.* **7**, 2001662 (2020).
- Wan, C. et al. An artificial sensory neuron with tactile perceptual learning. *Adv. Mater.* **30**, 1801291 (2018).
- Kim, Y. et al. A bioinspired flexible organic artificial afferent nerve. *Science* **360**, 998–1003 (2018).
- Shim, H. et al. Stretchable elastic synaptic transistors for neurologically integrated soft engineering systems. *Sci. Adv.* **5**, eaax4961 (2019).
- Lee, Y. R., Trung, T. Q., Hwang, B. U. & Lee, N. E. A flexible artificial intrinsic-synaptic tactile sensory organ. *Nat. Commun.* **11**, 2753 (2020).
- Park, H. L. et al. Retina-inspired carbon nitride-based photonic synapses for selective detection of UV light. *Adv. Mater.* **32**, 1906899 (2020).
- Mennel, L. et al. Ultrafast machine vision with 2D material neural network image sensors. *Nature* **579**, 62–66 (2020).
- Chen, J. Y. et al. Ultrafast responsive and low-energy-consumption poly(3-hexylthiophene)/perovskite quantum dots composite film-based photonic synapse. *Adv. Funct. Mater.* **31**, 2105911 (2021).
- Cheng, Z., Rios, C., Pernice, W. H. P., David Wright, C. & Bhaskaran, H. On-chip photonic synapse. *Sci. Adv.* **3**, e1700160 (2017).
- Lee, K. et al. Retina-inspired structurally tunable synaptic perovskite nanocones. *Adv. Funct. Mater.* **31**, 2105596 (2021).
- Wang, Y. et al. Stretchable temperature-responsive multimodal neuromorphic electronic skin with spontaneous synaptic plasticity recovery. *ACS Nano*. **16**, 8283–8293 (2022).
- Sun, L. et al. Synaptic computation enabled by Joule heating of single-layered semiconductors for sound localization. *Nano Lett.* **18**, 3229–3234 (2018).
- Guo, L. Q., Wen, J., Zhu, L. Q., Fu, Y. M. & Xiao, H. Humidity-dependent synaptic plasticity for proton gated oxide synaptic transistor. *IEEE Electron Device Lett.* **38**, 1248–1251 (2017).
- Nie, S., He, Y., Liu, R., Shi, Y. & Wan, Q. Low-voltage oxide-based synaptic transistors for spiking humidity detection. *IEEE Electron Device Lett.* **40**, 459–462 (2019).
- Kim, Y. et al. Bird-inspired self-navigating artificial synaptic compass. *ACS Nano* **15**, 20116–20126 (2021).
- Kim, H. Y. et al. Shape-deformable and locomotive MXene ($\text{Ti}_3\text{C}_2\text{T}_x$)-encapsulated magnetic liquid metal for 3D-motion-adaptive synapses. *Adv. Funct. Mater.* **33**, 2210385 (2022).
- Yu, J. et al. Contact-electrification-activated artificial afferents at femtojoule energy. *Nat. Commun.* **12**, 1581 (2021).
- Shan, L. et al. A sensory memory processing system with multi-wavelength synaptic-polychromatic light emission for multi-modal information recognition. *Nat. Commun.* **14**, 2648 (2023).
- Chen, Y. et al. Nanofloating gate modulated synaptic organic light-emitting transistors for reconfigurable displays. *Sci. Adv.* **8**, eabq4824 (2022).
- Chen, Q. et al. Neuromorphic display system for intelligent display. *Nano Energy* **94**, 106931 (2022).
- Deheyne, D. D. & Wilson, N. G. Bioluminescent signals spatially amplified by wavelength-specific diffusion through the shell of a marine snail. *Proc. R. Soc. B* **278**, 2112–2121 (2011).
- Ohmiya, Y., Kojima, S., Nakamura, M. & Niwa, H. Bioluminescence in the limpet-like snail, *Latia neritoides*. *Bull. Chem. Soc. Jpn.* **78**, 1197–1205 (2005).
- Lee, K. H. et al. ‘Cut and stick’ rubbery ion gels as high capacitance gate dielectrics. *Adv. Mater.* **24**, 4457–4462 (2012).
- Choi, Y., Oh, S., Qian, C., Park, J. H. & Cho, J. H. Vertical organic synapse expandable to 3D crossbar array. *Nat. Commun.* **11**, 4595 (2020).
- Lee, S., Lee, H. J., Ji, Y., Lee, K. H. & Hong, K. Electrochemiluminescent transistors: a new strategy toward light-emitting switching devices. *Adv. Mater.* **33**, 2005456 (2021).
- Guo, W. et al. Potential-resolved multicolor electrochemiluminescence for multiplex immunoassay in a single sample. *J. Am. Chem. Soc.* **140**, 15904–15915 (2018).
- Adamson, N. S. et al. Emission from the working and counter electrodes under co-reactant electrochemiluminescence conditions. *Chem. Sci.* **12**, 9770–9777 (2021).
- Rivnay, J. et al. High-performance transistors for bioelectronics through tuning of channel thickness. *Sci. Adv.* **1**, e1400251 (2015).

40. Furukawa, Y. & Shimokawa, D. Polarons, bipolarons, and electrical properties of crystalline conducting polymers. *Bull. Chem. Soc. Jpn.* **96**, 1243–1251 (2023).
41. Kachuee M., Fazeli S. & Sarrafzadeh M. ECG heartbeat classification: a deep transferable representation. In *2018 IEEE International Conference on Healthcare Informatics (ICHI)* 443–444 (IEEE, 2018).
42. Choi, S., Yang, J. & Wang, G. Emerging memristive artificial synapses and neurons for energy-efficient neuromorphic computing. *Adv. Mater.* **32**, 2004659 (2020).s

Publisher's note Springer Nature remains neutral with regard to jurisdictional claims in published maps and institutional affiliations.

Springer Nature or its licensor (e.g. a society or other partner) holds exclusive rights to this article under a publishing agreement with the author(s) or other rightsholder(s); author self-archiving of the accepted manuscript version of this article is solely governed by the terms of such publishing agreement and applicable law.

© The Author(s), under exclusive licence to Springer Nature Limited 2025

Methods

Materials

Processing solvents, acetone, 2-propanol and toluene were purchased from Sigma-Aldrich. PDMS (Sylgard 184) and its cross-linkers were purchased from Dow Corning. P3HT (weight-averaged molecular mass, $M_w = 50,000$ – $75,000$) with a regioregularity above 90%, P(VDF–HFP) ($M_w \approx 400,000$, number-averaged molecular mass, $M_n \approx 130,000$) and TPrA were purchased from Sigma-Aldrich. Additionally, [PYR₁₄][TFSI], Ru(bpy)₃Cl₂ and Ir(dFppy)₂(bpy) were purchased from TCI. Firpic was purchased from Ossila. The P3HT solution was prepared by dissolving it in toluene at a concentration of 10 mg ml⁻¹ and heating on a hot plate for 1 h at 65 °C to coat the semiconductor layer. The electrochemiluminescent ion gel solution was prepared by dissolving P(VDF–HFP) and [PYR₁₄][TFSI] in acetone at a 1:3.5:6.5 weight ratio. Subsequently, luminophores and TPrA were added to the solution, maintaining a weight ratio of 0.1 and 2, respectively, relative to the weight of P(VDF–HFP). First, P(VDF–HFP) was dissolved in acetone under continuous stirring at 65 °C for 2 h. Subsequently, [PYR₁₄][TFSI] was added to the solution, and the mixture was stirred at 65 °C for an additional 30 min. Subsequently, luminophores were introduced into the solution, stirring at 60 °C for 3 h. Finally, TPrA was added to the solution, and the temperature was lowered to 50 °C to prevent thermal degradation. The mixture was then stirred for 2 h before use. The entire process was carried out inside a glove box to minimize the humidity.

Device fabrication

A glass substrate was cleaned using an ultrasonic bath, first with acetone and subsequently with 2-propanol, each for 10 min. First, the ITO (60 nm thick) for the source/drain electrodes (channel length and width of 120 μm and 180 μm, respectively) was sputtered onto the cleaned substrate. Following the sputtering, the deposited ITO was patterned using photolithography to form the source/drain electrodes. Subsequently, the P3HT solution was spin-coated on the source/drain electrodes, employing a speed of 1,500 r.p.m. for 60 s. Heat treatment was administered at 150 °C for 10 min to enhance the P3HT mobility¹². The drop-casted ion gel was then transferred to the device. Drop-casting was performed on a hot plate at 50 °C. After 1 min, a PET film was floated on the solution to ensure a planar gel surface. Following heat treatment for 3 h and film removal, the remaining solvent was allowed to evaporate in ambient conditions for 12 h. Subsequently, the ion gel was transferred onto the P3HT using the cut-and-stick method. PDMS (mixed in a base and curing agent ratio of 10:1) was poured onto a dome-shaped Si mould and annealed at 80 °C for 12 h to facilitate hardening to fabricate the elastomeric top gate. Thereafter, 2 min 30 s of O₂ plasma treatment was applied to the moulded PDMS, and Cr/Au (3 nm/60 nm thick) was thermally evaporated onto the dome-shaped PDMS.

Device characterization

The cross-sectional morphology and elemental composition of the ECL-TVS device were analysed using a field-emission scanning electron microscope (JEOL-7800F) and energy-dispersive X-ray maps, respectively. Transistor properties and synaptic characteristics measurements were performed using a Keithley 4200 semiconductor characterization system and a semiconductor parameter analyser (4155C, Keysight) equipped with a pulse generator (81104A, Keysight). Pressure application and measurement were performed by utilizing z-axis pressure equipment, paired with force gauges. The luminance and ECL spectra of the devices were obtained using a spectroradiometer (Konica CS 2000). Numerical simulations of the electric field distribution within the device were conducted using the finite-element analysis software COMSOL Multiphysics 5.6 (COMSOL). The impedance of the ECL-TVS ion gels was measured via electrochemical impedance spectroscopy, sweeping through a frequency range from 100 Hz to 1 MHz, using a multichannel potentiostat (VMP2, BioLogic). Cyclic voltammetry was performed at a scan rate of 25 mV s⁻¹ using the same

multichannel potentiostat. Characterization of the crystallinity of the ECL-TVS ion gels was accomplished via grazing-incidence wide-angle X-ray scattering, performed at the PLS-II 9A U-SAXS beamline at the Pohang Accelerator Laboratory. The X-ray wavelength was set to 1.1069 Å, while the incident angle was modulated between 0.10° and 0.15°.

Electrochemical and spectroelectrochemical characterization

All liquid-electrolyte-based electrochemical measurements were performed using a BioLogic SP-200 potentiostat with a standard three-electrode system and acetonitrile solution with 0.1 M [PYR₁₄][TFSI] supporting electrolyte. P3HT thin films spin-coated on ITO-coated glass substrates, Ag/Ag⁺ wire filled with 0.01 M AgNO₃ and 0.1 M tetrabutylammonium perchlorate, and a coiled platinum wire were employed as the working, reference and counter-electrodes, respectively. For spectroelectrochemical measurements, a Keen Innovative Solutions OPTIZEN POP UV–vis spectrometer was employed. The beam path passed through an electrolyte-filled quartz glass cuvette containing the polymer/ITO/glass working electrode. A background spectrum of the cell without external bias was recorded before in situ spectroelectrochemical measurements.

Development of hand recognition and video brightness extraction algorithms

Hand recognition and video brightness extraction algorithms were developed within the Google Colab environment. For the hand recognition algorithm, modifications were made to the source code provided by Google MediaPipe, leveraging its robust framework for hand-tracking applications. The video brightness extraction algorithm involved uploading videos to the Colab environment for efficient video processing and brightness analysis in the cloud. Further technical details, including the configurations and adjustments made to the algorithms, can be found in Supplementary Figs. 29 and 34. The code for these algorithms is available upon request from the corresponding author.

Fabrication and set-up of the wearable ECL-TVS device

Three elastomeric finger caps with hemispherical gold-coated PDMS top gates were fabricated and fitted on the index, middle and ring fingers (Fig. 4a). The ECL-TVSs were designed to emit red, green and blue ECL corresponding to the bending motions of the index, middle and ring fingers, respectively. A 7.5 cm × 5 cm panel device integrating three ECL-TVSs was developed and mounted onto a palm for secure placement (left inset, Fig. 4a). Lightweight finger caps made from a commercial rubber film with an elastomeric hemispherical top were also prepared for ease of use (right inset, Fig. 4a). To precisely control the tactile contact area during exercises, a 2-mm-diameter hole was introduced into each ECL-TVS using masking tape (right inset, Fig. 4a).

Preparation of dataset for arrhythmia monitoring task

The MIT-BIH arrhythmia dataset contains ECG recordings from 47 subjects, each independently annotated by two or more cardiologists. On the basis of the AAMI EC57 standard, the annotations can be categorized into five classes (Supplementary Table 3). The MIT-BIH dataset was first preprocessed with a 125 Hz sampling frequency to evaluate the monitoring capability of the suggested SNN. All data were cropped and downsampled to ensure the same dimension, such that each ECG signal contained 187 data points with normalized amplitudes ranging from 0 to 1 over timesteps.

Arrhythmia monitor based on an SNN with ECL-TVS

For arrhythmia monitoring, we designed a SNN comprising 187 pre-neurons, 935 synapses and 5 post-neurons. The network initialized all the w to 0.1 and then assigned each class to each post-neuron.

To encode ECG signals into spikes, pre-neurons utilized a Gaussian neuron model as follows:

$$g_i(x) = \frac{1}{\sigma\sqrt{2\pi}} \exp\left(-\frac{(x-\mu_i)^2}{2\sigma^2}\right), \quad (1)$$

where

$$\mu_i = x_{\min} + (x_{\max} - x_{\min}) \frac{i}{n-1}, \text{ for } i = 0, \dots, n-1. \quad (2)$$

Here, x , n and σ are the input, the number of populations at each pre-neuron and the s.d. n and σ were set to be 10 and 0.25. Although the number of pre-neurons is effectively increased by n (in our case, $187 \times 10 = 1,870$), this population encoding scheme can facilitate temporal precision and the neuronal variability problem of temporal coding by spreading each input over multiple pre-neurons. Note that constants n and σ can be further optimized. The Gaussian pre-neurons sparsely generated either one or no spikes in response to an input. If a relatively strong input is applied to the pre-neuron, the spike latency required to generate one spike (t_{pre}) becomes shorter. Conversely, a relatively weak input makes t_{pre} longer. An example of the spike encoding scheme using Gaussian pre-neurons is presented in Supplementary Fig. 41.

On the basis of the set of t_{pre} and w , when the weighted spikes were delivered into post-neurons, their membrane potentials ($V(t)$) over timestep (t) changed according to the leaky integrate-and-fire neuron model:

$$V(t + \Delta t_n) = V(t) + \frac{\Delta t_n}{\tau_n} (-V(t) + R I_n(t)), \quad (3)$$

where constants τ_n , R and Δt_n were set to be 6, 5 and 0.01, while $I_n(t)$ represents the weighted input at t . If $V(t)$ at a certain post-neuron exceeds a threshold of 3.5, the post-neuron fires an output spike at a timestep t_{post} , as shown in Fig. 5b.

For the SNN learning, we employed a two-step learning process: (1) the supportive step and (2) the STDP learning step. The supportive step aims to adjust initial w values to a certain set to enhance the effect of subsequent STDP learning. For example, a post-neuron receives either its corresponding or non-corresponding ECG class; w values were updated to increase (that is, reward) or decrease (that is, penalize) by Δw , respectively, on the basis of t_{pre} :

$$\Delta w = C(1 - t_{\text{pre}}), \quad (4)$$

where constant C was set to be 4. Moreover, the penalty is evenly distributed over inactive synapses connected to non-spiking pre-neurons by $\Delta w/N_{\text{inactive}}$, where N_{inactive} is the number of inactive synapses. Note that inactive synapses that have an initial w value are excluded, and the minimum w was set to the initial w . An example of the supportive step is provided in Supplementary Fig. 42. STDP learning was then performed on the basis of $\Delta t = t_{\text{post}} - t_{\text{pre}}$, mathematically expressed as

$$\Delta w = A_{\pm} \exp\left(\frac{\Delta t}{\tau_{\pm}}\right), \quad (5)$$

where fitting parameters A_{\pm} and τ_{\pm} with respect to different pressures are presented in Supplementary Table 4. The w values connected to pre-neurons that generate spikes before their corresponding post-neuron fires are strengthened according to experimental STDP curves, and vice versa. We used 200 and 50 ECG signals for learning and diagnosis, respectively. Note that diagnostic accuracy can be further improved by learning the network with a larger dataset instead of device optimization and changing the SNN framework.

Data availability

The data that support the findings of this study or additional data related to this study are available from the corresponding author upon reasonable request. Source data are provided with this paper.

Acknowledgements

This study was supported by the Creative Materials Discovery Program and the Pioneer Research Centre Program through the National Research Foundation of Korea (NRF) funded by the Ministry of Science, ICT & Future Planning (NRF-2022M3C1A3081211), by a grant from the National Research Foundation of Korea (NRF) funded by the Korean government (MEST) (RS-2023-00208577), by the Nano & Material Technology Development Program through the National Research Foundation of Korea (NRF) funded by the Ministry of Science and ICT (RS-2024-00451891 and RS-2024-00416938), and by the Open Resource Research Program of the Korea Institute of Science and Technology (2E32961). This study was also supported by the National R&D Program administered by the National Research Foundation of Korea (NRF) of the Korea government (Grant NO. RS-2024-00407271, RS-2023-00220077 and RS-2024-00342191) and Korea University Research Grant.

Author contributions

W.K. and K.L. conceived and designed the experiments. S.C. performed and analysed neural network simulations. E.P. performed the spectroelectrochemical measurement on the P3HT film. G.K. performed the fabrication and demonstration of the ECL-TVS and prepared the figures. J. Ha assisted in some of the experiments, including ion gel preparation and electrical characterization. Yeeun Kim, J.J., J.H.O. and H.K. performed ECL spectra, scanning electron microscopy and X-ray photoelectron spectroscopy measurements and prepared brightness extraction algorithm developments. T.K. and Yeonji Kim assisted with the characterization of ECL ion gel properties. K.-N.K., W.J. and J.Y. prepared a brightness extraction algorithm. A.J. advised on the optical measurements and analyses. J. Hong and D.R. devised a rehabilitation treatment protocol and advised on the relevant content. T.-W.L. and K.K. participated in the discussions regarding the experimental results and provided an interpretation of them. G.W. and C.P. supervised the project, analysed the data and wrote the manuscript. All authors discussed the results and commented on the study.

Competing interests

The authors declare no competing interests.

Additional information

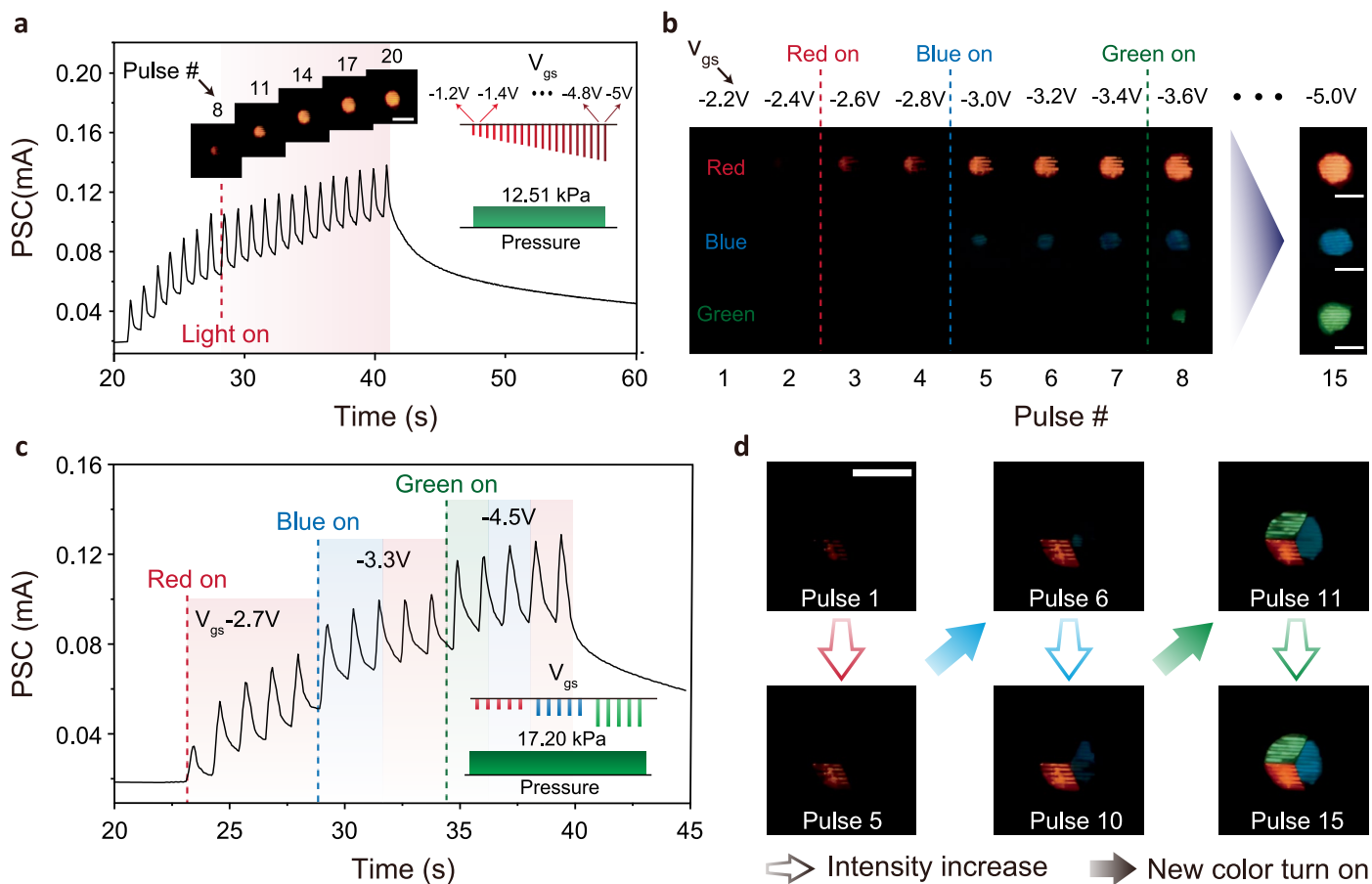
Extended data is available for this paper at <https://doi.org/10.1038/s41563-025-02124-x>.

Supplementary information The online version contains supplementary material available at <https://doi.org/10.1038/s41563-025-02124-x>.

Correspondence and requests for materials should be addressed to Gunuk Wang or Cheolmin Park.

Peer review information *Nature Materials* thanks Paschalis Gkoupidenis, Qijun Sun and the other, anonymous, reviewer(s) for their contribution to the peer review of this work.

Reprints and permissions information is available at www.nature.com/reprints.



Extended Data Fig. 1 | Full-colour ECS-TVS. (a) A plot of the PSC response of an R-ECL-TVS, utilising 20 V_{gs} pulses sequentially increasing in magnitude. The inset photographs display the light emission of R-ECL-TVS at the increasing number of V_{gs} pulses. scale bar: 5 mm. (b) Photographs of R, G, and B-ECL-TVS with continuous 15 gate voltage pulses, sequentially increasing in magnitude from -2.2 V to -5 V. Scale bar: 3 mm. (c) Plot of the PSC response of integrated R-,

G-, and B-ECL-TVS, utilising 15 gate voltage pulses comprising three sets of five voltage pulses with different voltage magnitudes (-2.7 V for five pulses, -3.3 V for five pulses, and -4.5 V for five pulses) under pressure of 17.20 kPa. (d) Photographs of integrated R-, G-, and B-ECL-TVS at the 1st, 5th, 6th, 10th, 11th, and 15th V_{gs} pulses. Scale bar: 5 mm.